



Constructing built-in electric field in Co/Co₉S₈ heterojunction encapsulated in N, S co-doped carbon polyhedron for high-efficiency oxygen electrocatalysis

Ping Bai, Peng Wang, Jiarong Mu, Yihua Zhao, Chunfang Du, Yiguo Su^{*}

Inner Mongolia Key Laboratory of Chemistry and Physics of Rare Earth Materials, College of Chemistry and Chemical Engineering, Inner Mongolia University, Hohhot 010021, China

ARTICLE INFO

Keywords:

Co/Co₉S₈ junction
Built-in electric field
Oxygen reduction reaction
Oxygen evolution reaction
Zn-air battery

ABSTRACT

Achieving a subtle equilibrium between the activity and durability of transition metal chalcogenides (TMCs) towards oxygen reduction (ORR) and oxygen evolution (OER) reactions remains a formidable challenge. Therefore, we present a built-in electric field (BEF) tactic to build Co/Co₉S₈ heterojunctions with larger work function difference ($\Delta\Phi$) as bifunctional electrocatalysts for high-efficiency zinc-air batteries (ZABs). Impressively, Co/Co₉S₈@NSC shows a higher half-wave potential ($E_{1/2}$) of 0.88 V for ORR and a lower overpotential ($E_{j=10}$) of 137 mV at 10 mA·cm⁻² for OER. Moreover, ZABs based on Co/Co₉S₈@NSC electrocatalysts exhibit an impressive power density of 267.83 mW·cm⁻² and robust cyclability over 1000 h at 10 mA·cm⁻². The experiments and theoretical studies elucidate that the interface-induced electric field effect facilitates the redistribution of interfacial charge, thereby improving the covalency of the Co-S bond. Additionally, it effectively promotes charge transfer and optimizes adsorption of oxygen intermediate in both ORR and OER.

1. Introduction

The sluggish dynamics of oxygen reduction (ORR) and oxygen evolution (OER) reactions have emerged as a significant bottleneck in the advancement of zinc-air batteries (ZABs) as sustainable energy storage solutions [1–4]. Unfortunately, the application of highly successful commercially viable precious metal electrocatalysts such as Pt-based and Ir-based electrocatalysts on a large-scale is hindered by their exorbitant cost and limited availability [5]. Hence, the development of highly efficient and steady electrocatalysts based on non-noble metals is critical.

The transition metal chalcogenides (TMCs) electrocatalysts with tunable electron structure and controlled morphology have confirmed excellent OER activity under alkaline medium but limited ORR activities. The ORR activity is closely correlated with the discharge efficiency of ZABs. However, the primary factors contributing to the low ORR activity of TMCs include a limited number of active sites, inadequate electrical conductivity, and unsuitable adsorption strength towards oxygen intermediates [6–8]. Moreover, the OER, closely associated with the charging process of ZABs, exhibits a highly oxidizing nature, and possesses the capability to readily trigger TMCs reconstruction. The

reconstruction of TMCs often results in the cleavage of the chemical bond between sulfur and low-cost metals, leading to the gradual conversion of TMCs into oxyhydroxides with reduced conductivity, accompanied by the leaching of sulfur [9,10]. As a result, the charge transfer kinetics and the lifetime of the TMCs are both reduced in this situation. The reconstruction and agglomeration of TMCs during long-term operation of the TMCs-based ZABs typically lead to decreased adhesion between the catalyst and substrate, resulting in catalyst loss [11]. Therefore, the aforementioned issues leading to diminished ORR activity and compromised OER stability for TMCs remain the primary impediments hindering their ability to deliver exceptional bifunctional performance that meets the practical requirements of ZABs.

The formation of built-in electric field (BEF) at the interface, consisting of hetero components with distinct crystal structures and work functions, spontaneously occurs [12–15]. This phenomenon regards as an efficient approach to facilitate charge transfer, achieve charge balance, and modulate the adsorption intensity of oxygen intermediates [16–19]. For instance, the ZnS/NiCo₂S₄ heterojunctions including enormous interfaces. The findings revealed that the presence of a built-in interfacial potential can enhance the thermodynamic formation of *O to *OOH, thereby improving their intrinsic activity [20]. The

^{*} Corresponding author.

E-mail address: cesyg@imu.edu.cn (Y. Su).

<https://doi.org/10.1016/j.apcatb.2024.123882>

Received 22 January 2024; Received in revised form 19 February 2024; Accepted 23 February 2024

Available online 25 February 2024

0926-3373/© 2024 Elsevier B.V. All rights reserved.

studies that have been reported on $\text{Co}_9\text{S}_8/\text{NS-C}$ heterojunction show that the cooperative effect between Co_9S_8 layers and NS-C efficiently control the Fermi levels, leading to an increased adsorption capacity for oxygen intermediates in $\text{Co}_9\text{S}_8/\text{NS-C}$ compared with pure Co_9S_8 and NS-C [21]. Besides activity improvement by the implementation of the BEF strategy, the long term stability of TMCs-based ZABs should also be concerned, which is crucial to its commercial requirements. The electronegativity of sulfur in TMCs is significantly higher than that of transition metals, leading to reduced covalency of M-S bonds. Therefore, to achieve electron density balance between metal and S atom by constructing BEF to induce electron redistribution is a feasible strategy to improve the covalency of M-S bonds. However, the coupling of TMCs with other components, such as transition metals and their oxides, leads to severe localization of charge carriers because of the overlapped electron clouds at the interface of metal-oxygen. In this region, electrons are typically delocalized through-metal while protons are confined within the oxide. As a result, orientation becomes uncontrollable and there is even a reduction in BEF strength. The work function (Φ) represents the minimal amount of energy needed to move electrons from the Fermi level to the vacuum level, thus enabling control over charge transport direction at the interface by adjusting $\Delta\Phi$ between hetero components [22,23]. Based on the aforementioned research, it is possible and reasonable to regulate the adsorption of intermediates and improve the covalency of M-S bonds by carefully selecting suitable hetero components with appropriate work functions for constructing and controlling the BEF. Furthermore, given the intricate nature of oxygen electrocatalysis involving multiple adsorption/desorption steps of reactants, intermediates, and products occurring at the active site, thus enhancing the mass transfer performance of TMCs-based heterojunction electrocatalysts is crucial to ensure their efficient and stable operation in ZABs. The molecular sieve imidazole salt frameworks (ZIF-8 and ZIF-67) are considered suitable templates for obtaining highly stable metallic carbon materials due to their high metal content and abundant C species [24]. Moreover, the polyhedral structure of the functional carbon formed after pyrolysis exhibits a significant surface area and favorable internal channels, thereby facilitating efficient mass transfer during both ORR and OER processes [25]. And the incorporation heteroatoms into the ZIF-derived carbon materials facilitates enhanced electronic interaction between metal active sites and the carbon polyhedron, thereby bolstering the catalytic activity of carbon materials [26,27]. Furthermore, N, S codoped carbon materials not only contain non-metallic active species such as C-N and C-S-C, but also exhibit abundant surface carbon defects that could modulate the electronic structure of the carbon matrix and boost its conductivity [28].

Herein, $\text{Co}/\text{Co}_9\text{S}_8$ heterojunction uniformly anchored on the surface of N, S codoped carbon materials were prepared by a partial vulcanization-pyrolysis approach. The optimized $\text{Co}/\text{Co}_9\text{S}_8/\text{NSC}$ catalyst surpasses the performance of commercial noble-metal benchmarks, exhibiting a higher $E_{1/2}$ value of 0.88 V for the ORR and a lower $E_{\text{j}=10}$ value of 137 mV for the OER in alkaline media. Moreover, rechargeable ZABs employing $\text{Co}/\text{Co}_9\text{S}_8/\text{NSC}$ as an air cathode demonstrate exceptional performance including high-power density of $267.83 \text{ mW}\cdot\text{cm}^{-2}$, specific discharge capacity of $806.7 \text{ mAh}\cdot\text{g}^{-1}$ at $10 \text{ mA}\cdot\text{cm}^{-2}$, and remarkable cycling stability with ultralong lifespans exceeding 1000 h at $10 \text{ mA}\cdot\text{cm}^{-2}$. The analysis of Kelvin probe force microscopy and X-ray photoelectron spectroscopy (XPS) reveal that the construction of BEF promotes electron transfer from Co to Co_9S_8 , thereby obtaining a balanced electron density of Co-S bonds. The XPS results after stability testing reveal that the leaching of S from $\text{Co}/\text{Co}_9\text{S}_8/\text{NSC}$ in the OER process was effectively inhibited, which can be largely due to the interfacial electron rearrangement induced by BEF, thereby boosting the covalent property of Co-S bonds. Due to the electropositivity and lower Φ value of Co [29,30], when constructing $\text{Co}/\text{Co}_9\text{S}_8$ heterostructure, the electrons will be transferred from Co to Co_9S_8 . It was expected that Co would induce interfacial electron redistribution to balance the electron density between the Co and S element in Co_9S_8 . This ultimately

strengthened the covalency of the Co-S bond. The results obtained from density functional theory (DFT) further confirm that the electron contribution from Co atom effectively regulates the electronic density of both Co and S, thereby enhancing the covalency of Co-S bonds. In addition, the difference in work function ($\Delta\Phi$) induces a strong BEF, which enhances charge movement and provides feasible adsorption intensity for oxygen intermediates, thereby improving the catalytic performance of ORR.

2. Experimental section

2.1. Catalyst preparation

2.1.1. Preparation of $\text{Co}_9\text{S}_8/\text{NSC}$ and $\text{Co}/\text{Co}_9\text{S}_8/\text{NSC}$

The typical setup involved placing a quartz boat containing an as-prepared ZIF-8@ZIF-67 precursor sample at the outlet end, while thiourea was positioned at the intake end within the central region of the tube furnace. The mixture was calcined at a temperature of 900°C for 2 h under the N_2 . By adjusting the mass ratio of ZIF-8@ZIF-67-3: thiourea (1:0.3, 1:0.5, 1:0.7 and 1:0.9), both partial and complete vulcanization of Co could be achieved. The ZIF-8@ZIF-67-3: thiourea mass ratio of 1:0.5 (denoted as $\text{Co}/\text{Co}_9\text{S}_8/\text{NSC-2}$) was selected for investigating the mechanism and evaluating the performance in Zn-air batteries.

2.2. Material characterization

The X-ray diffraction (XRD) technique was employed to analyze the crystal structure of catalysts at 40 KV. The morphology and element distribution of the catalysts were conducted using scanning electron microscopy (SEM, Hitachi S-4800) and transmission electron microscopy (TEM, FEI Tecnai G² F20 S-TWIN) combined with energy dispersive spectroscopy (EDS). The X-ray photoelectron spectroscopy (XPS, British company Kratos) technique was employed for the detection and analysis of element composition and valence. The contents of element were conducted using inductively coupled plasma-atomic emission spectrometry (ICP-AES).

2.3. Electrocatalytic measurements

The electrocatalytic measurements were conducted using a CHI760 electrochemical workstation. A glassy carbon electrode (GCE, 0.193 cm^2) used as the work electrode. 5 mg of catalyst was evenly scattered in a mixture of ethanol (0.1 mL) and Nafion solution (10 μL , 0.5 wt%) to form a suspension. The catalyst ink (5.0 μL) was dropped onto a GCE using pipette (1.0–10.0 μL). The catalyst loadings on glassy-carbon were $0.5 \text{ mg}\cdot\text{cm}^{-2}$ for Co/NSC , $\text{Co}_9\text{S}_8/\text{NSC}$, $\text{Co}/\text{Co}_9\text{S}_8/\text{NSC-1}$, $\text{Co}/\text{Co}_9\text{S}_8/\text{NSC-2}$ and $\text{Co}/\text{Co}_9\text{S}_8/\text{NSC-3}$.

3. Results and discussion

3.1. Theoretical insights of boosting covalency of Co-S bond by the construction of the $\text{Co}/\text{Co}_9\text{S}_8$ heterojunction

The feasibility of introducing metallic Co to enhance the stability of Co-S bonds in Co_9S_8 was investigated through DFT analysis. The charge transfer ability at the interface was closely associated with the relative electron escape difficulty from the junction surface, and the Φ value determined the feasibility and direction of electron

transfer. A lower Φ value indicated easier electron escape from the metal site [22,31]. Therefore, we first employed DFT to calculate the Φ values of each heterogeneous component in $\text{Co}/\text{Co}_9\text{S}_8$ heterojunction. The calculated results indicated that the Φ values for Co and Co_9S_8 were conducted to be 4.040 and 4.571 eV (Fig. 1a, b). As a result, the construction of a heterojunction between Co and Co_9S_8 was expected to result in a rebalancing of the electron population, driven by the

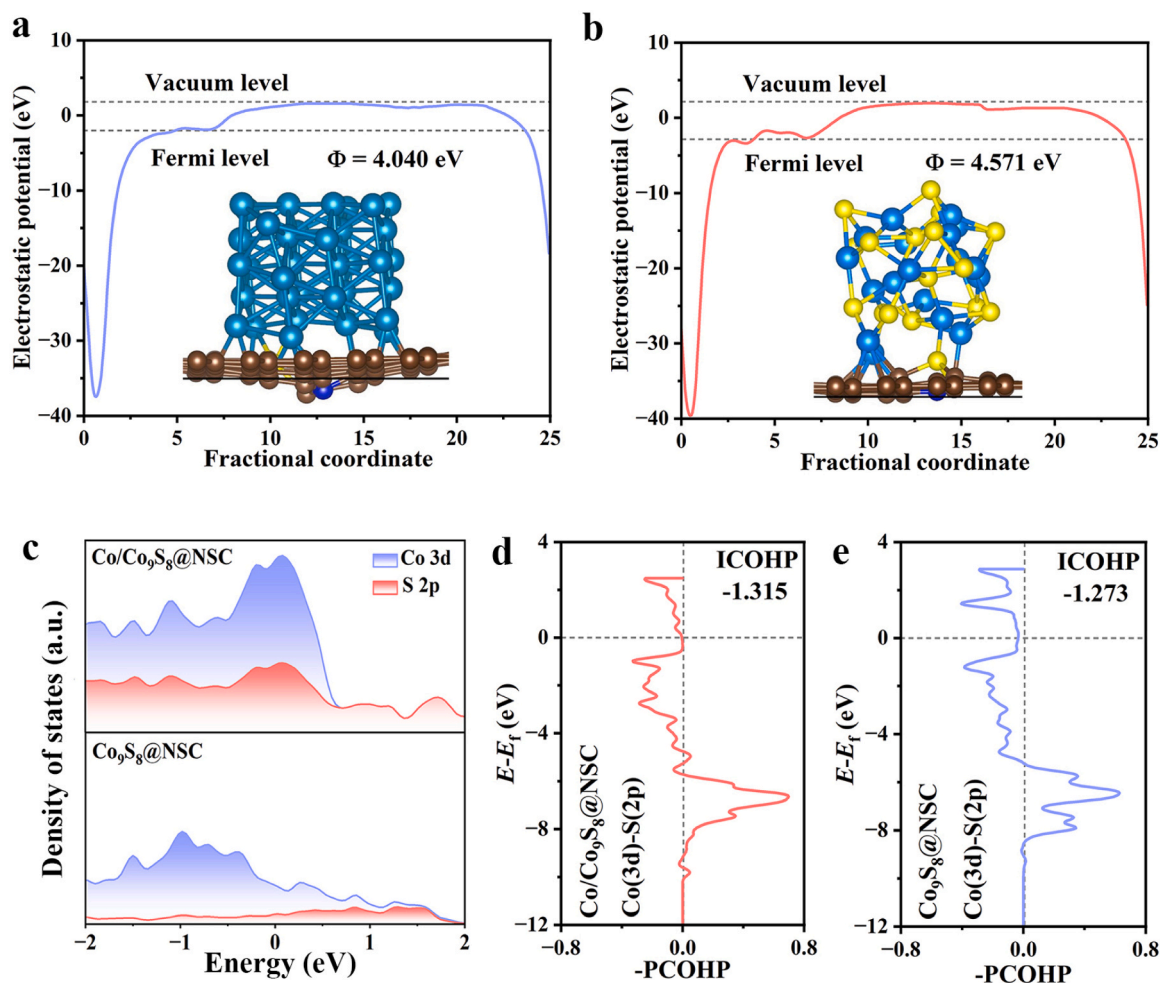


Fig. 1. Work function calculation of (a) Co@NSC and (b) Co₉S₈@NSC. (c) The PDOS for the Co 3d and S 2p of Co₉S₈@NSC and Co/Co₉S₈@NSC. (d, e) The projected COHP for the Co-S interactions in Co₉S₈@NSC and Co/Co₉S₈@NSC.

difference in work function, thereby effectively regulating the interfacial electron density. As shown in Fig. S1, a significant charge redistribution was observed at the heterogeneous interface of Co/Co₉S₈, with electrons being transferred from Co to Co₉S₈, which revealed a pronounced charge redistribution at the heterogeneous interface of Co/Co₉S₈.

In addition, the density of states shown in Fig. 1c demonstrated a stronger overlap between the Co 3d and S 2p orbits in Co/Co₉S₈@NSC by comparison with Co₉S₈@NSC. This suggested an increased binding strength between Co and S atoms in Co/Co₉S₈@NSC, highlighting the significant role of metallic Co in enhancing the covalency. Moreover, the strength differences of the Co-S bond in Co/Co₉S₈@NSC and Co₉S₈@NSC were further analyzed using the crystal orbital Hamilton population (COHP). A more negative ICOHP value indicated a stronger Co-S bond. Hence, the higher ICOHP value observed for the Co-S bond of Co/Co₉S₈@NSC in Fig. 1d, e provided supporting evidence for their improved stability compared to individual Co₉S₈@NSC. The aforementioned results demonstrated that the formation of the Co/Co₉S₈ heterojunctions with large $\Delta\Phi$ could induce interfacial electron redistribution and facilitate electron transfer from Co to Co₉S₈. This phenomenon contributed to the equilibration of electron density within the Co-S bond, thereby enhancing the covalency of the Co-S bond in Co₉S₈.

3.2. Synthesis and structural characterization of Co/Co₉S₈@NSC-2

The polyhedral Co/Co₉S₈@NSC catalyst was synthesized using a two-step method (Fig. 2a). The ZIF-8@ZIF-67 was fabricated through seed epitaxial growth due to the identical crystal structures, unit-cell

parameters of ZIF-8 ($a = 16.9910$ Å) [32] and ZIF-67 ($a = 16.9589$ Å) [33], as confirmed by XRD analysis (Fig. S2a). Subsequently, the Co/Co₉S₈@NSC sample was synthesized via a facile thermostatic

reduction strategy. During calcining process, the thiourea acted as a sulfide trigger to control the fabrication of Co/Co₉S₈ heterostructures. The XRD patterns displayed that Co@NSC, Co₉S₈@NSC and a series of Co/Co₉S₈@NSC with good crystallization and various phase component could be obtained by regulating the Co/S ratio (Fig. 2b and Fig. S2b). As exhibited in Fig. 2b, three diffraction peaks of Co/Co₉S₈@NSC-2 at 44.2° , 51.5° and 75.9° corresponded to the (111), (200) and (220) crystal planes of Co (JCPDS: 15-0806) [34], while two relatively weak peaks at 29.8° and 52.1° could be ascribed to the (311) and (440) crystal faces of Co₉S₈ (JCPDS: 86-2273) [35], indicating the formation of Co/Co₉S₈@NSC heterostructure. With increase of the thiourea ($x=0.3, 0.5, 0.7$ and 0.9 , Table S1), the product finally gradually transformed from Co/Co₉S₈@NSC into Co₉S₈@NSC. Furthermore, the TEM image suggested that Co/Co₉S₈@NSC-2 was composed of small-scale nanoparticles and a thin shell (Fig. 2c). HRTEM images of Co/Co₉S₈@NSC-2 (Figs. 2d and 2e) showed the fringe spacing of 0.21 and 0.29 nm, being ascribed to the (111) and (311) planes of Co and Co₉S₈, respectively. The presence of defects in the carbon layer promoted electron transfer, thereby enhancing the catalytic performance of the electrocatalyst [21, 36]. Particularly, a distinct interface between Co and Co₉S₈ could be observed, verifying the successful build of the Co/Co₉S₈@NSC-2 heterojunction. The elemental mapping indicated an evenly distribution of Co, S, C and N elements throughout the entire Co/Co₉S₈@NSC-2 structure (Fig. 2f-g). In addition, we also displayed microstructure of

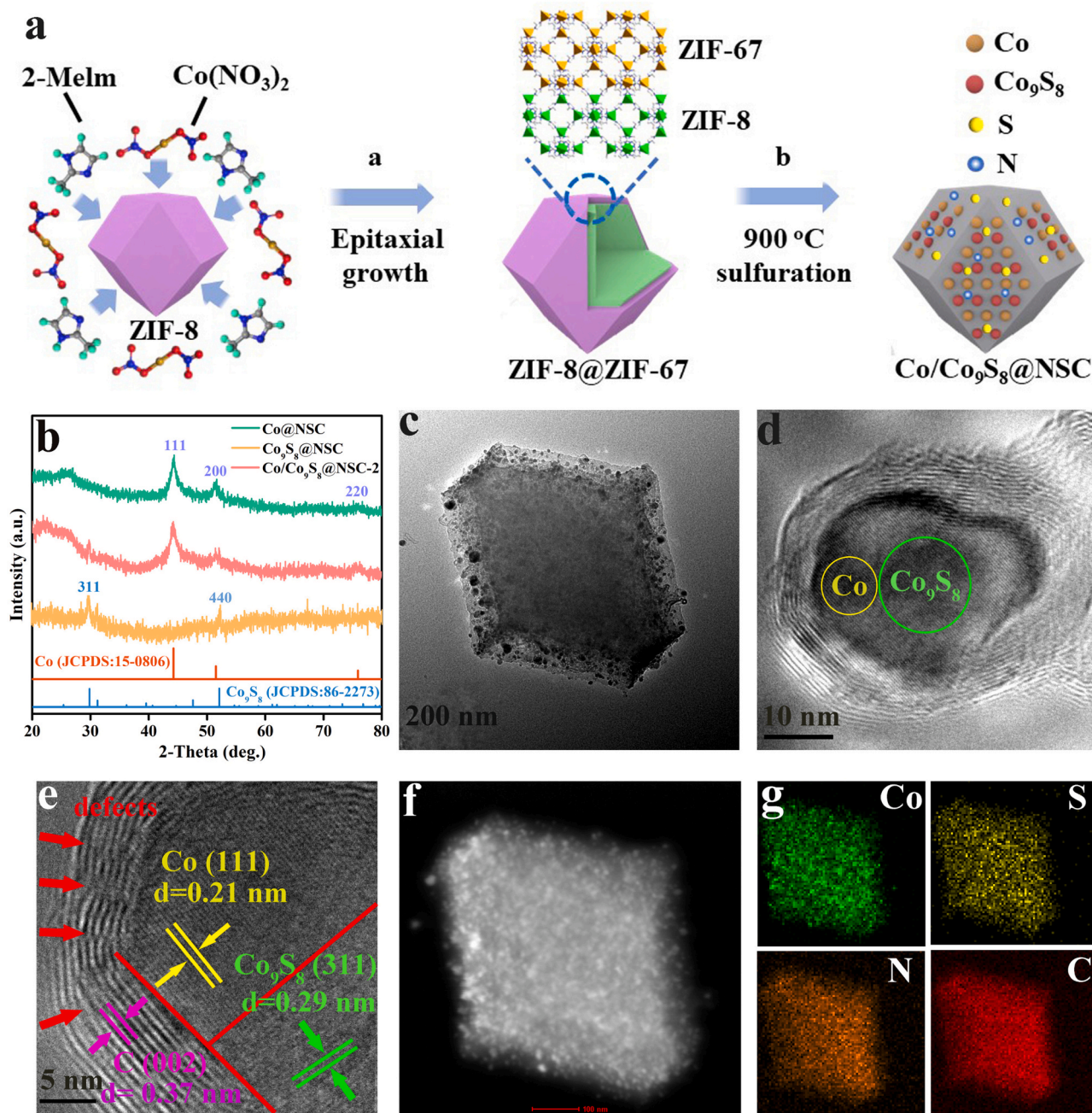


Fig. 2. (a) Schematic diagram of the synthesis of Co/Co₉S₈@NSC catalyst. (b) XRD patterns of the Co@NSC, Co₉S₈@NSC and Co/Co₉S₈@NSC-2. (c) TEM image, (d-e) HRTEM images, (f) HAADF-STEM image and (g) elemental mapping analysis of as-obtained Co/Co₉S₈@NSC-2.

ZIF-8@ZIF-67-3 (Zn:Co molar ratio of 1:3) sample (Fig. S3), which performed rhombic dodecahedral core-shell structures with remarkably polished surface.

The electronic structure of Co@NSC, Co₉S₈@NSC and Co/Co₉S₈@NSC-2 samples was investigated by XPS. The full spectra, as illustrated in Fig. S4a, confirmed the coexistence of Co, N, C and S elements in Co/Co₉S₈@NSC-2. The four observed peaks at 777.9/793.3 eV, 779.6/795.2 eV, 781.3/797.2 eV and 784.3/800.5 eV could be attributed to the metallic Co, Co³⁺, Co²⁺ and satellite peaks [37], respectively, indicating the coexistence of Co₉S₈ and metallic Co in the Co/Co₉S₈@NSC-2 (Fig. 3a). Compared to Co₉S₈@NSC, the Co 2p_{3/2} peaks of

Co/Co₉S₈@NSC-2 exhibited negative shifts (0.26 eV), suggesting an augmentation in electron density surrounding the Co after forming a heterostructure [38–40]. Conversely, the peak of Co 2p_{3/2} in

Co/Co₉S₈@NSC-2 shifted towards a higher binding energy (0.23 eV) compared with Co@NSC, suggesting a reduction in electron density of Co. These results indicated the introduction of Co induced charge rearrangement at the Co/Co₉S₈@NSC-2 interface, thereby promoting the charge transfer from Co to Co₉S₈ [41]. Moreover, the C 1s spectrum (Fig. 3b) displayed three prominent peaks at 284.4, 284.8 and 288.5 eV, which could be attributed to C=C, C-C, and O=C-O, respectively [22, 42]. And the peak observed at 285.8 eV could be attributed to the C-N/C-S, indicating successful doping of N and S into the carbon framework (Fig. 3b) [43]. In addition, the S 2p peak located at 162.5 eV could be ascribed to Co-S_x, which confirmed the formation of Co₉S₈ in the Co/Co₉S₈@NSC-2. Meanwhile, the two peaks located at 163.7 and 164.9 eV were ascribed to the C-S-C, indicating that the presence of S was doped in the carbon framework. And the peak observed at 168.2 eV corresponded to the C-SO_x-C [22]. The of S 2p for Co/Co₉S₈@NSC-2

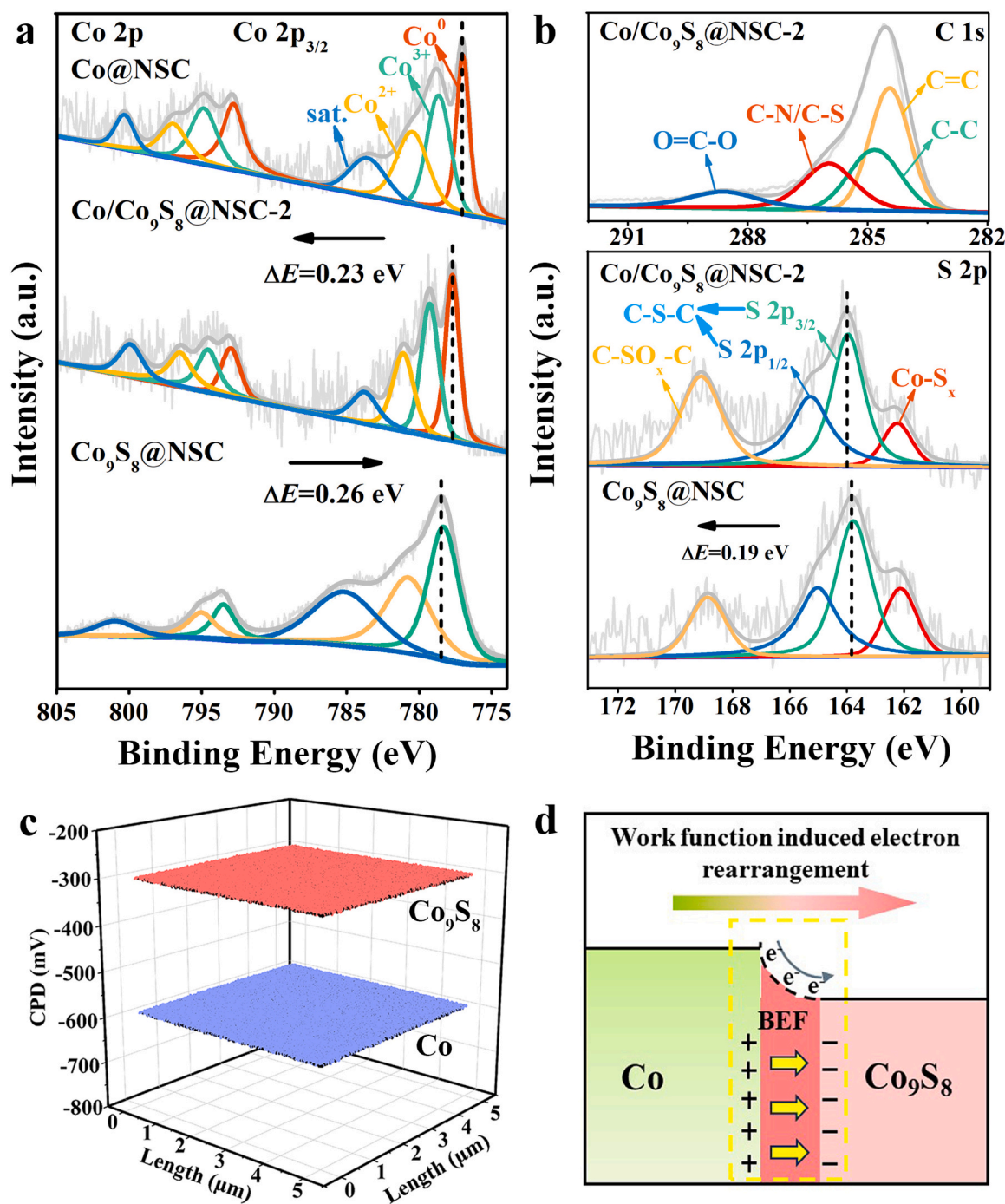


Fig. 3. XPS spectra of (a) Co 2p, (b) C 1s and S 2p of Co@NSC, Co₉S₈@NSC and Co/Co₉S₈@NSC-2. (c) Contact potential differences of Co₉S₈ and Co relative to a gold reference. (d) Charge transfer process in Co/Co₉S₈@NSC-2.

displayed a positive shift compared with Co₉S₈@NSC, suggesting a reduction in electron density of S. These completely-opposed variation in electron cloud density of Co and S after forming the BEF in Co/Co₉S₈@NSC-2 further indicated that the introduced Co could enhance the covalent property of the Co-S bonds by adjusting the electron cloud density, thereby impeding their damage in the OER. The XPS researches were in line with the DFT calculative results. The N 1s spectrum of Co/Co₉S₈@NSC-2 displayed five distinct nitrogen species, namely pyridinic N (398.2 eV), Co-N_x (399.1 eV), pyrrolic N (400.1 eV), graphitic N (401.2 eV) and oxidation state N (403.1 eV) [44,45], as shown in Fig. S4b. Remarkably, in comparison with Co@NSC and Co₉S₈@NSC, the content of pyridinic N (38.4%) and graphitic N (12.5%)

in Co/Co₉S₈@NSC-2 was found to be higher (Table S2), which had been confirmed to as efficient active sites for improving ORR and OER performance [46,47]. The aforementioned observation further supported the evidence that N was doped within the carbon framework. As displayed in Fig. 3c and Fig. S5, the contact potential difference (CPD) between Co, Co₉S₈ and the gold probe was -0.6 V and -0.3 V, respectively. Therefore, the Φ of Co and Co₉S₈ were conducted to be 4.1 and 4.4 eV, respectively, by the formula of Φ (eV) = $4.7 + e \times \text{CPD}$ [48]. Accordingly, a BEF would build when coupled together, inducing the electron flow from high level to low until the system achieved an equilibrium (Fig. 3d). The BEF with monodirectional charge transfer could balance the charge, which could concurrently drive the

electron-abundant Co area and electron-insufficient Co₉S₈ region, thus improving the adsorption of oxygen intermediates [49,50].

3.3. Electrode activity and durability analyses

To confirm the concept that we presented, we evaluated the bifunctional electrocatalytic performance (ORR/OER) of the Co/Co₉S₈@NSC-2 catalyst in 0.1 M KOH solution, together with Co@NSC, Co₉S₈@NSC, Co/Co₉S₈@NSC-1 and Co/Co₉S₈@NSC-3 for comparison. Preliminary results suggested that ZIF-8@ZIF-67-3 displayed optimal electrocatalytic OER performance (Fig. S6). Their heterogeneous hybridization rendered superior bifunctional catalytic properties and durability to transition metal chalcogenides toward ORR/OER and their

coupled process, which were hardly attainable by the catalysts from single MOF precursor [51]. Polarization (Fig. 4a, S7a) and Tafel curves (Fig. 4b, S7b) indicated that OER performance of Co/Co₉S₈@NSC with various Co/S ratio and IrO₂. Specifically, Co@NSC and Co₉S₈@NSC possessed an optimal ratio balance point to collectively provide the most effective OER sites. As depicted in Fig. 4c, when the Co:S ratio as 1:0.5, the OER

activity of Co/Co₉S₈@NSC-2 reached the highest (overpotential @10 mA·cm⁻² = 137 mV; Tafel slope = 45 mV·dec⁻¹), better than pure Co@NSC and Co₉S₈@NSC, suggesting that the kinetic process of OER was markedly optimized after formation of the heterostructure. Compared with other Co-based heterostructure catalysts, Co/Co₉S₈@NSC-2 also exhibited the outstanding OER performance (Fig. 4d

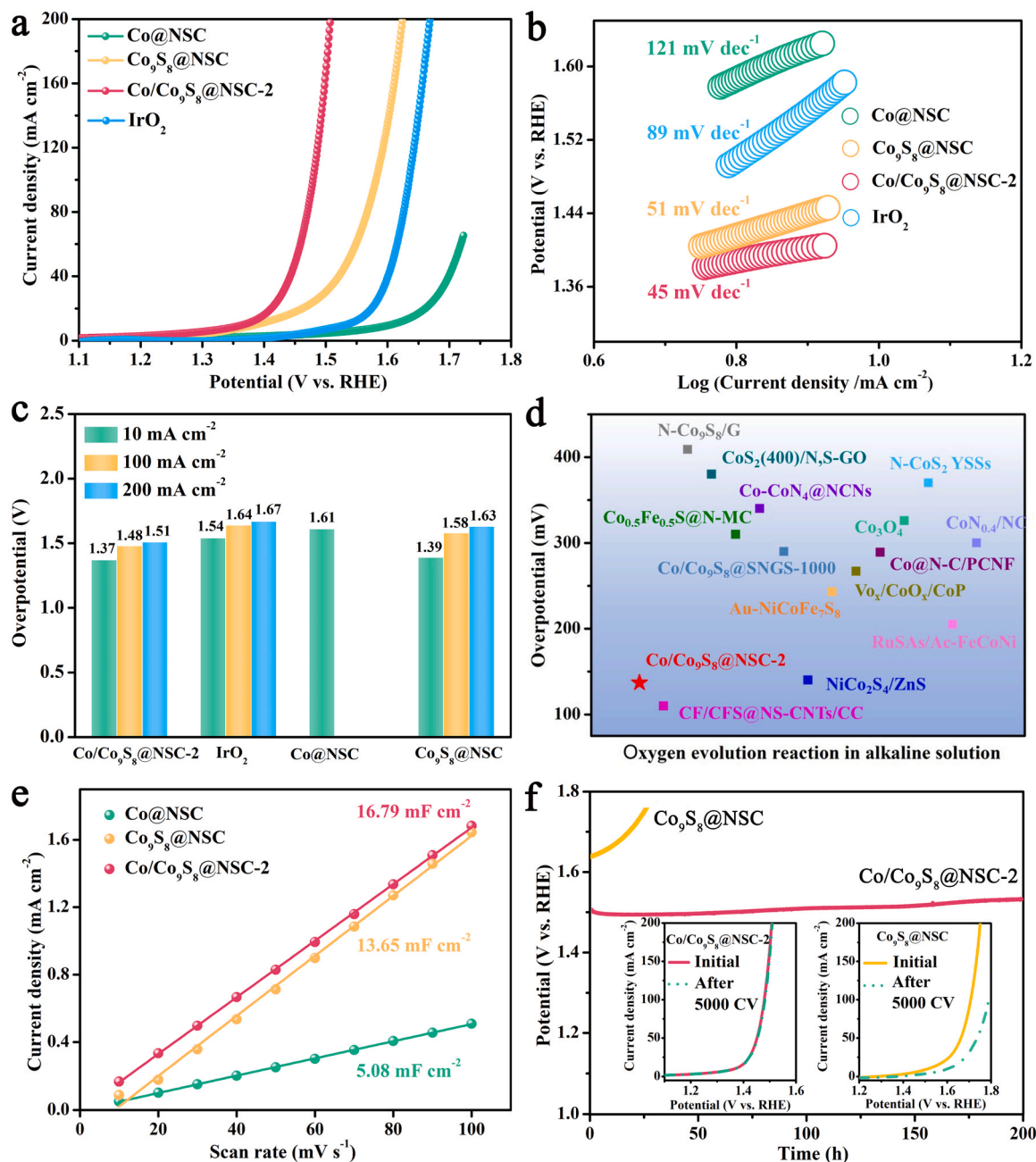


Fig. 4. (a, b) LSV curves and Tafel plots, (c) overpotentials required to deliver current densities of 10, 100 and 200 mA·cm⁻² for Co@NSC, Co₉S₈@NSC, Co/Co₉S₈@NSC-2 and IrO₂ catalysts. (d) Comprehensive comparison of the performance of Co/Co₉S₈@NSC-2 and other representative state-of-the-art catalysts. (e) C_{dl} curves for Co@NSC, Co₉S₈@NSC and Co/Co₉S₈@NSC-2. (f) Chronopotentiometric durability test (inset images displayed cycling stability tests of Co/Co₉S₈@NSC-2 and Co₉S₈@NSC).

and Table S4). Moreover, the elements related to the enhanced activity of Co/Co₉S₈@NSC-2 in 0.1 M KOH were further explored. As displayed in Fig. 4e and Fig. S7 c-h, Co/Co₉S₈@NSC-2 also possessed the largest electrochemical double-layer capacitance (C_{dl} , 16.79 mF·cm⁻²), implying exposure of a greater deal of active sites densities at the Co/Co₉S₈@NSC-2 heterostructure [51,52]. The C_{dl} of Co₉S₈@NSC without Co support showed a remarkable decrease compared to Co/Co₉S₈@NSC-2, suggesting the serious occlusion of reachable active sites. In the meantime, the EIS testing (Fig. S7 i) further revealed a distinct improvement in the Rct of Co₉S₈@NSC compared with Co/Co₉S₈@NSC-2. Moreover, the ECSA-normalized specific activity (j_{ECSA}) was acquired and was displayed in Fig. S8. Co/Co₉S₈@NSC-2 showed a higher intrinsic activity with $j_{ECSA} = 1.31$ mA·cm⁻² at 1.55 V

(vs. RHE), which was approximately 7.3 times higher than that of Co₉S₈@NSC. This further confirmed the key role of the interface-induced electric field effect between Co and Co₉S₈ for enhancing the electrocatalytic performance. The stability of the sample was also a vital indicator for evaluating its performance. As shown in Fig. 4f, the Co/Co₉S₈@NSC-2 displayed almost parallel curve about 200 h at 200 mA·cm⁻². However, the potential of Co₉S₈@NSC without Co support exhibited an obvious augment after about 20 h under resembled testing. The excellent durability of Co/Co₉S₈@NSC-2 was further confirmed by the nearly overlapping LSV curves examined after 5000 cycles (inset of Fig. 4f), while an obvious reduction could be observed in the LSV of Co₉S₈@NSC. That indicated that Co₉S₈@NSC without Co

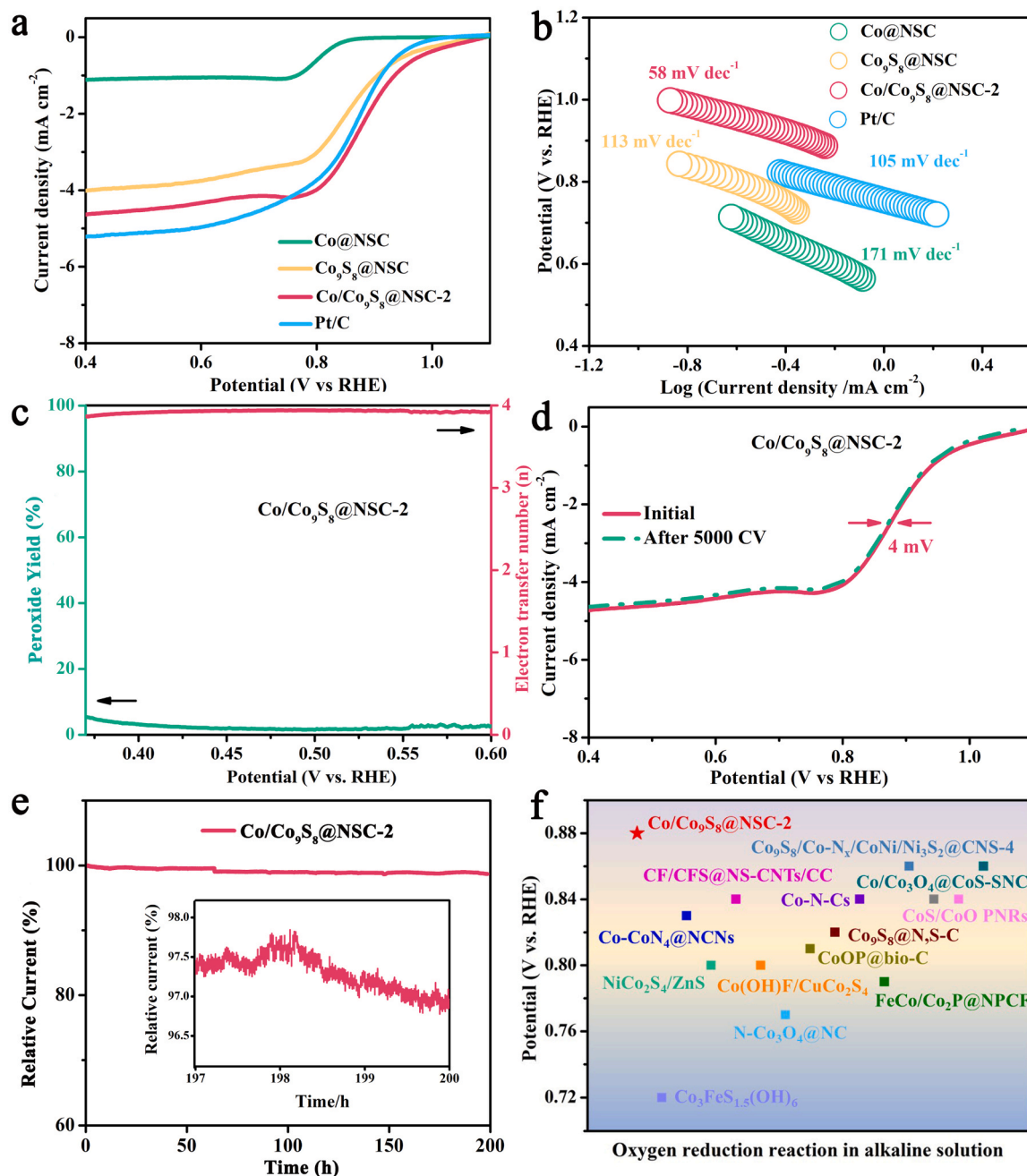


Fig. 5. (a) LSV measurements of ORR in 0.1 M KOH solution at 1600 rpm; (b) Tafel plots of the Co@NSC, Co₉S₈@NSC, Co/Co₉S₈@NSC-2 and Pt/C catalysts. (c) Percentage of peroxide and the corresponding electron transfer number n ; (d) ORR polarization curves before and after the durability experiment for 5000 cycles; (e) chronoamperometric curves of Co/Co₉S₈@NSC-2. (f) Comparison of half-wave potential of Co/Co₉S₈@NSC-2 and recently reported other representative ORR catalysts.

support underwent uncontrollable phase transformation because of configurable instability in the process of strong oxidation, thereby damaging its electron transfer ability [53].

Moreover, the ORR activity of samples was conducted in 0.1 M KOH solution. The LSV curves in Fig. 5a exhibited that Co/Co₉S₈@NSC-2 with the built-in electric field displayed superior half-wave potential ($E_{1/2}$) of 0.88 V compared with Co₉S₈@NSC ($E_{1/2}$ = 0.87 V), commercial Pt/C ($E_{1/2}$ = 0.86 V) and other controllable catalysts (Fig. S9a). The Co/Co₉S₈@NSC-2 sample, as described in Fig. 5b and Fig. S9b, exhibited a smaller Tafel slope of 58 mV·dec⁻¹ compared with Co@NSC, Co₉S₈@NSC and Pt/C, indicating that the existence of Co dramatically enhanced the ORR kinetics for Co/Co₉S₈@NSC-2. The favorable evidence provided by the LSV and Tafel curves supported the significant part of Co in promoting the ORR performance. The disk and ring currents of the Co/Co₉S₈@NSC-2 sample (Fig. 5c and Fig. S9c) indicated an exceptional catalytic selectivity for ORR towards hydroxide ions (OH⁻) through a highly efficient four-electron ORR process, as evidenced by the average H₂O₂ yield of 4.12% and calculated electron transfer number of 3.95. Furthermore, the stability of the Co/Co₉S₈@NSC-2 was evaluated through chronoamperometric curves and accelerated durability tests (ADT). The $E_{1/2}$ value of Co/Co₉S₈@NSC-2 only decreased by 4 mV (Fig. 5d) during the ORR process, which was dramatically better than Pt/C (21 mV, Fig. S9d). And the Co/Co₉S₈@NSC-2 demonstrated a retention rate of 96.8% of its original current after 200 h test, as

illustrated in Fig. 5e. This further highlighted the remarkable stability of Co/Co₉S₈@NSC-2. Notably, the outstanding ORR performance of Co/Co₉S₈@NSC-2 exceeded a majority of other Co-based catalysts (Fig. 5f, Table S5). Furthermore, the TEM images of Co/Co₉S₈@NSC-2 after ADT of ORR confirmed that the N, S co-doped carbon polyhedron exhibited a retained morphology (Fig. S10), revealing that H₂O₂ did not etch the carbon support. Furthermore, the XPS measurement was applied to determine the element content. Fig. S11 and Table S3 showed that the content of C for Co/Co₉S₈@NSC-2 showed no obvious alteration before (90.79 wt%) and after (90.73 wt%) ADT of ORR, further indicating that H₂O₂ did not etch the carbon support. After conducting the ORR stability test, the XRD patterns, XPS spectra and TEM image (Fig. S12) further provided evidence that the cycled Co/Co₉S₈@NSC-2 catalyst maintained its composition and morphology almost unchanged compared to the initial Co/Co₉S₈@NSC-2 sample. The excellent durability of the Co/Co₉S₈@NSC-2 sample could be credited to the BEF and N, S co-doped carbon polyhedron, which effectively hindered the corrosion of Co/Co₉S₈ NPs resulting from direct contact with the electrolyte during the ORR process. The N, S codoped carbon polyhedron coating strategy also effectively enhanced both the stability and activity of the bifunctional catalysts [54]. With appropriate high-temperature treatment, ZIF-8@ZIF-67 could undergo in-situ controllable transformation into metal/metal sulfide nanoparticles coated with N, S codoped carbon. The N, S codoped carbon polyhedron in such a hybrid architecture was

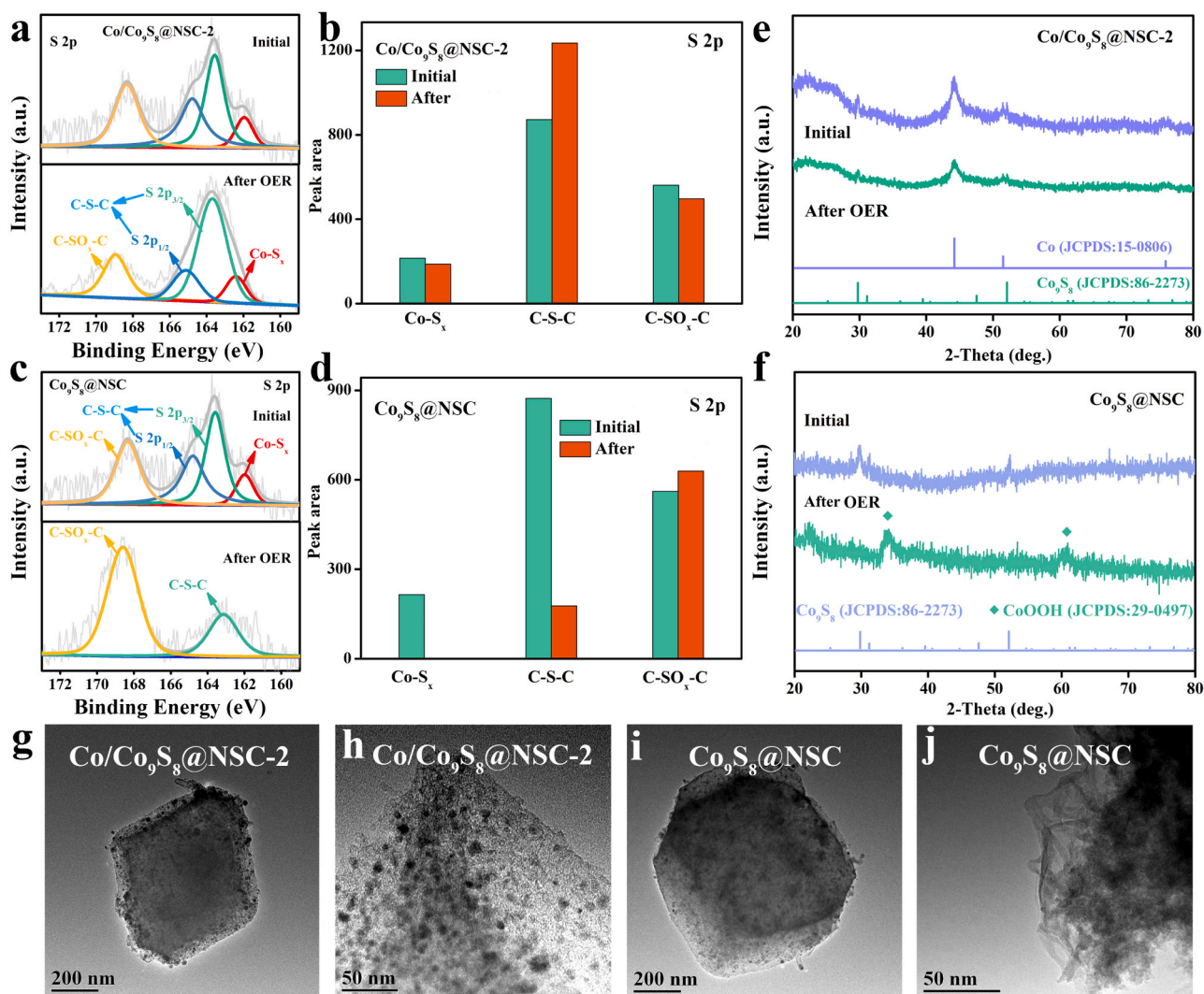


Fig. 6. (a-d) the XPS spectra and the peak areas of S 2p before and after OER stability testing. (e, f) The XRD patterns, (g-j) TEM images of after OER stability testing of Co/Co₉S₈@NSC-2 and Co₉S₈@NSC.

believed to provide protection against acid/alkaline corrosion for metal/metal sulfide nanoparticles, thereby extending their lifespan [55].

3.4. Recognition of distinct differences in durability between $\text{Co}_9\text{S}_8@\text{NSC}$ and $\text{Co}/\text{Co}_9\text{S}_8@\text{NSC-2}$ catalysts

The difference of stability between $\text{Co}_9\text{S}_8@\text{NSC}$ and $\text{Co}/\text{Co}_9\text{S}_8@\text{NSC-2}$ samples was researched by performing XPS, XRD and TEM analyses after 200 h OER

durability testing. The XPS spectrum of S 2p after durability test (Fig. 6a-d) revealed the complete disappearance of characteristic peaks associated with the Co-S bond in $\text{Co}_9\text{S}_8@\text{NSC}$, suggesting that the Co-S bond had been disrupted, potentially due to the full conversion of CoS

to CoOOH in $\text{Co}_9\text{S}_8@\text{NSC-2}$. After 5000 CV, the introduction of barium nitrate into the electrolyte resulted in the formation of a distinct precipitate, suggesting that the S atom from $\text{Co}_9\text{S}_8@\text{NSC}$ dissolved in the electrolyte to form sulfate during the reconstruction process (Fig. S13). However, the XPS spectra of Co-S_x (peak area) of $\text{Co}/\text{Co}_9\text{S}_8@\text{NSC-2}$ was almost unchanged after the stability test. Moreover, the XRD patterns (Fig. 6e, f) achieved after durability testing revealed the disappearance of characteristic peaks corresponding to Co_9S_8 in $\text{Co}_9\text{S}_8@\text{NSC}$, while the characteristic peaks connected with Co_9S_8 were well-preservative in $\text{Co}/\text{Co}_9\text{S}_8@\text{NSC-2}$. Meanwhile, the TEM images obtained after the stability testing revealed a transformation of Co_9S_8 NPs into low-crystallinity CoOOH . However, the Co_9S_8 NPs in $\text{Co}/\text{Co}_9\text{S}_8@\text{NSC-2}$ exhibited no distinct alternation after cycling (Fig. 6g-j). The above results

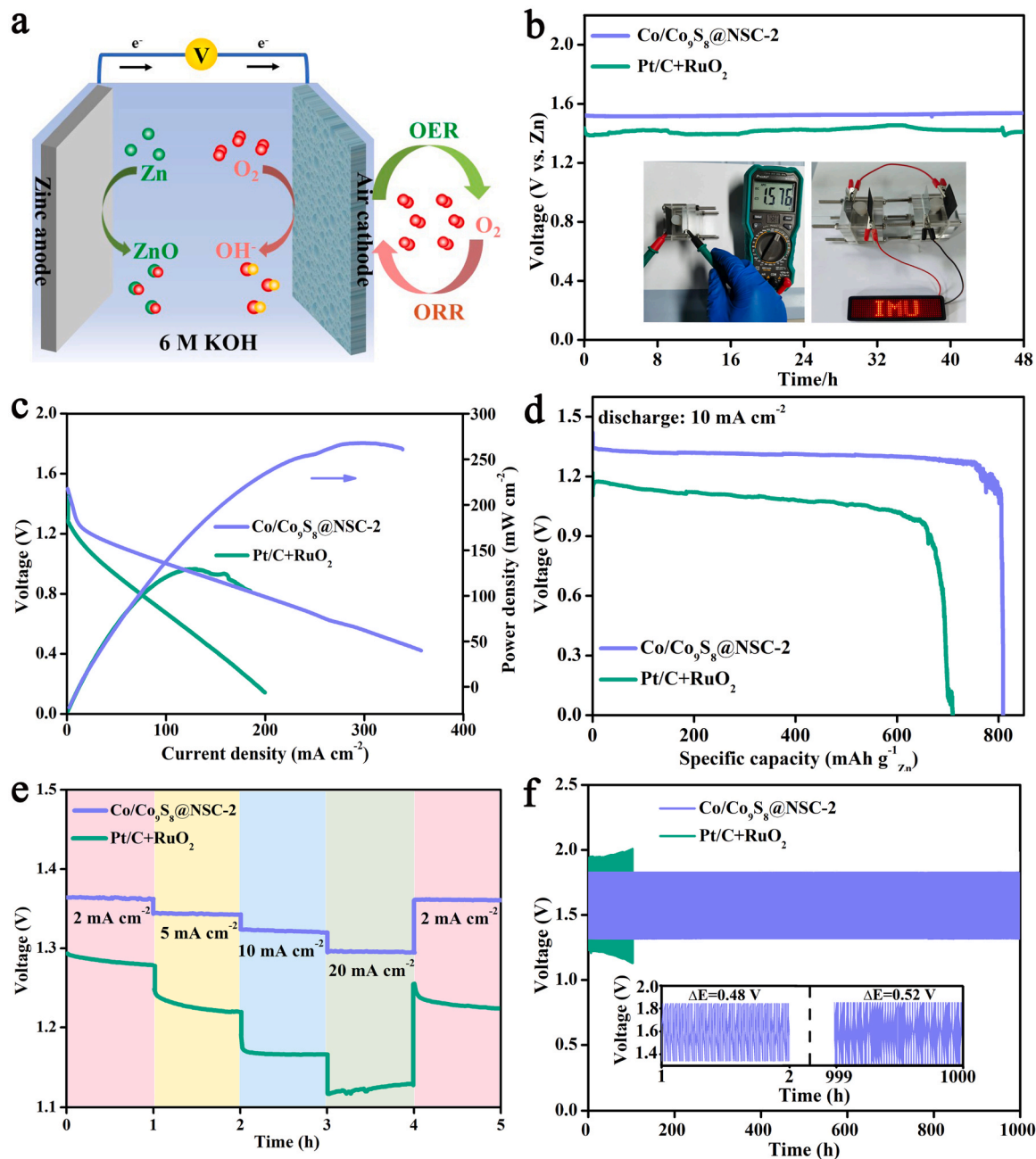


Fig. 7. (a) Schematic diagram of rechargeable ZAB with $\text{Co}/\text{Co}_9\text{S}_8@\text{NSC-2}$ catalyst. (b) Open-circuit plots (inset image showed photo of LEDs driven by two rechargeable ZABs in series with $\text{Co}/\text{Co}_9\text{S}_8@\text{NSC-2}$ catalyst), (c) power density plots, (d) discharge polarization curves at the current density of 10 mA cm^{-2} , (e) discharge curves of the battery at various current densities, (f) galvanostatic cycling stability of the rechargeable $\text{Co}/\text{Co}_9\text{S}_8@\text{NSC-2}$ and Pt/C+RuO_2 based ZABs at 10 mA cm^{-2} .

demonstrated that the interface-induced electric field effect effectively inhibited the leaching of S in Co/Co₉S₈@NSC and prevented excessive reconstruction of Co₉S₈ in Co/Co₉S₈@NSC, which was in agreement with the DFT calculations.

3.5. Application of electrocatalyst in zinc-air battery

Since the Co/Co₉S₈@NSC-2 sample displayed outstanding bifunctionality, a rechargeable ZAB was home-made with Co/Co₉S₈@NSC-2, Zn plate and KOH (6 M) for applications (Fig. 7a). A referential battery was also constructed for contrast using a traditional Pt/C+RuO₂ sample (Pt/Ru 1:1 mass ratio) as the air cathode. The open circuit voltage (OCV) of the Co/Co₉S₈@NSC-2 was 1.576 V, mildly higher than that of Pt/C+RuO₂ (1.440 V), being close to the theoretical voltage of ZABs

(1.65 V) (Fig. 7b and Fig. S14) [56]. And a LED screen could be driven by two Co/Co₉S₈@NSC-2 ZABs in series. Based on the discharge curve, the power density of Co/Co₉S₈@NSC-2 was calculated to be 267.83 mW·cm⁻² (Fig. 7c and Fig. S15), which was more than 2 times that of Pt/C+RuO₂ (121.53 mW·cm⁻²) and outperformed other reported cobalt-based electrocatalysts (Table S6), suggesting that Co/Co₉S₈@NSC-2 possessed superior recharging capability. The specific capacity was then conducted. The Co/Co₉S₈@NSC-2 generated a large specific capacity of 806.7 mAh·g⁻¹ at 10 mA·cm⁻²

(Fig. 7d), higher than that of Pt/C+RuO₂ (682.7 mAh·g⁻¹), based on the quality of consumed Zn. Moreover, the discharge rate capability of Co/Co₉S₈@NSC-2 was further confirmed by contrasting discharge voltages at different current densities of 2–20 mA·cm⁻². The Co/Co₉S₈@NSC-2 possessed a weaker voltage decrease tendency than Pt/

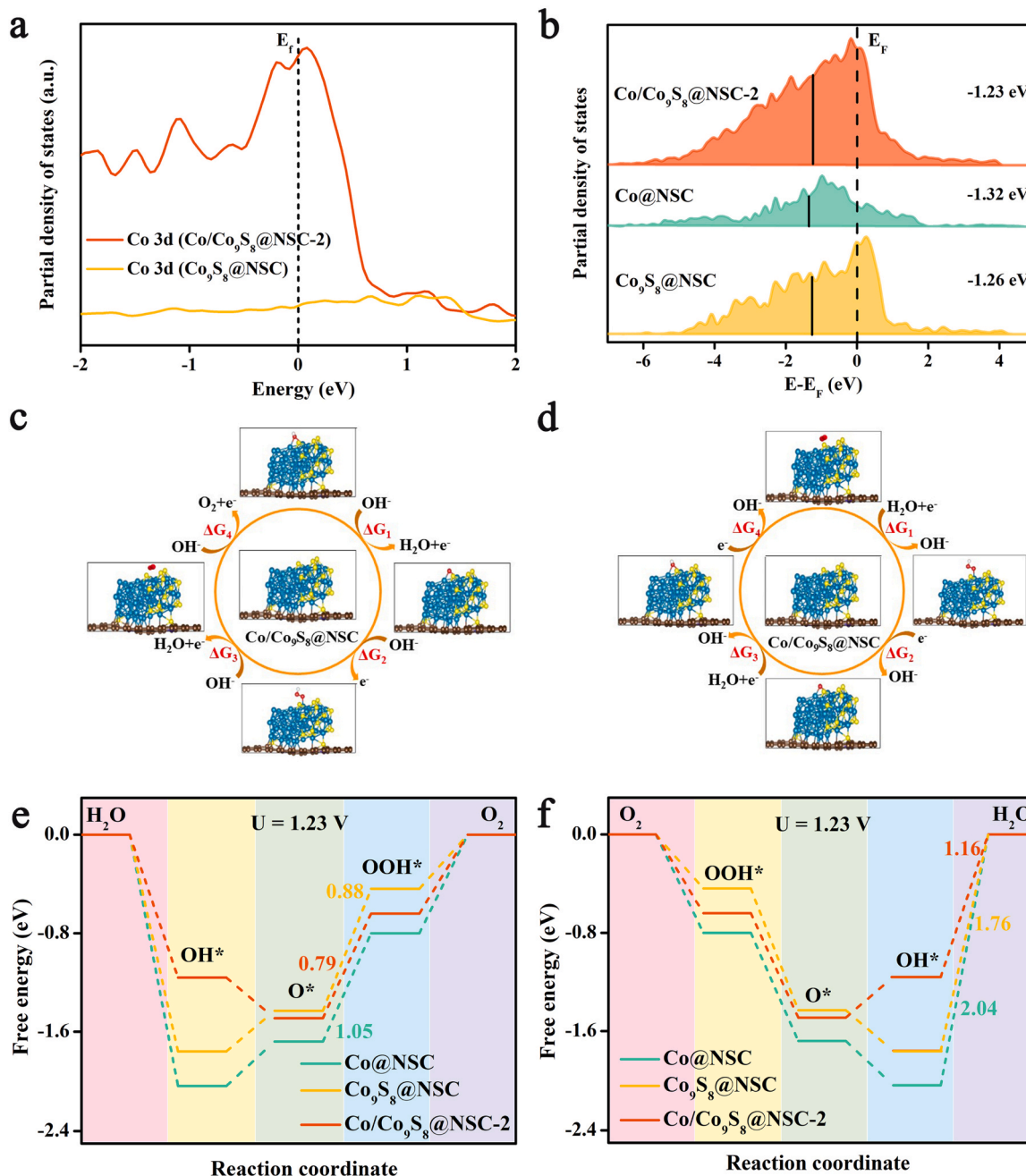


Fig. 8. (a) The PDOS for the Co 3d of Co/Co₉S₈@NSC-2 and Co₉S₈@NSC. (b) d-band center of Co@NSC, Co₉S₈@NSC and Co/Co₉S₈@NSC-2. (c, d) Configuration of the adsorption intermediates for Co/Co₉S₈@NSC-2. (e) Free-energy diagram for the OER process at the equilibrium potentials of $U = 1.23$ V and (f) Free-energy diagram for the ORR process at the equilibrium potentials of $U = 1.23$ V.

C+RuO₂ at various discharge current densities, suggesting that Co/Co₉S₈@NSC-2 had higher invertibility and durability (Fig. 7e). To assess the stability of the ZAB of Co/Co₉S₈@NSC-2, the battery was cycled for 1000 h at 10 mA·cm⁻². As exhibited in Fig. 7f, Co/Co₉S₈@NSC-2 achieved a much more stable discharge-recharge voltage gap (from 0.48 to 0.52 V) after 1000 h. And the voltage difference between the charge and discharge potentials exhibited a significant increase (0.89 V) after 100 h for Pt/C+RuO₂ battery, leading to the termination of the cycle measurement. This observed phenomenon was attributed to serious polarization effect [57], suggesting that the stability of Pt/C+RuO₂ catalyst was inadequate. The remarkable electrocatalytic performance and stable cycling of Co/Co₉S₈@NSC-2 in rechargeable ZABs could be largely attributed to the formation of an interfacial BEF between Co and Co₉S₈ in Co/Co₉S₈@NSC-2.

3.6. Investigating the potential reaction mechanism of inherent activity improvement for Co/Co₉S₈@NSC-2

The potential reaction mechanisms for the improved inherent activity of Co/Co₉S₈@NSC-2 were performed by DFT calculations. Due to the introduction of Co, the strength of the Co 3d orbit in Co/Co₉S₈@NSC-2 at the Fermi level (E_f) surpasses that of Co₉S₈@NSC (Fig. 8a), indicating an increased involvement of electrons in the reaction. This facilitates accelerated charge transfer and enhances conductivity. Electronic interaction at the interface could tune the location of d band center (ϵ_d) and impact the oxygen intermediates [58]. The ϵ_d values of Co@NSC and Co₉S₈@NSC were calculated as -1.32 and -1.26 eV, respectively (Fig. 8b), suggesting deficient oxygen intermediates [59]. However, the Co/Co₉S₈@NSC-2 exhibited an appropriate ϵ_d of -1.23 eV, which was conducive to the improvement adsorption of oxygen intermediates for improved performance. Calculative results confirmed that the electronic structure Co₉S₈@NSC could be regulated through the introduction of Co, leading to enhanced adsorption strength of reaction intermediates. The Gibbs free energy (ΔG) was a significant indicator for evaluating electrocatalytic activity [60]. The four fundamental steps of the most excellent OER and ORR intermediates of the relevant samples were schematically displayed in Fig. 8c, d and Fig. S16. The ΔG values of Co/Co₉S₈@NSC-2 during the OER (0.79 eV) and ORR (1.16 eV) were proportionally lower than those of Co₉S₈@NSC (Fig. 8e, f). The above results indicated that the interface-inducing electric field effect can effectively enhance charge transfer, promote the excellent adsorption capacity of oxygen intermediates of both ORR and OER.

4. Conclusions

In summary, Co/Co₉S₈ heterojunction encapsulated in N, S co-doped carbon polyhedron (Co/Co₉S₈@NSC) were resoundingly synthesized and demonstrated as high-efficiency bifunctional electrocatalysts for ZABs. The Co/Co₉S₈@NSC catalyst displays a half-wave potential of 0.88 V for ORR in an alkaline medium, while achieving an overpotential of 137 mV at 10 mA·cm⁻² for OER, surpassing both commercial Pt/C and IrO₂ catalysts. Moreover, a high-performance rechargeable Zn-air battery is achieved, exhibiting a high power density of 267.83 mW·cm⁻² and ultralong lifespans of 1000 h at a current density of 10 mA·cm⁻². This activity exceeds that observed in the majority of documented TMCs. The experiments and DFT results demonstrate that the work function difference ($\Delta\Phi$) conducted powerful interfacial BEF can result in interfacial electron redistribution, extracting electrons from nearby metallic Co sites to enhance the covalent property of Co-S bonds in Co₉S₈ by tuning the electron cloud density. This significantly mitigates the leaching of S from Co/Co₉S₈@NSC, ensuring the long-term stability of the Co/Co₉S₈@NSC catalyst. Moreover, The Co/Co₉S₈@NSC heterogeneous interface in the catalyst exhibits a remarkable synergistic effect, thereby boosting the charge movement and reducing the energy barrier for both ORR and OER. The research

provides beneficial perspectives into achieving a harmonious equilibrium between the activity and durability of bifunctional electrocatalysts based on TMCs.

CRediT authorship contribution statement

Chunfang Du: Methodology, Investigation, Formal analysis, Data curation, Conceptualization. **Yihua Zhao:** Investigation, Data curation. **Jiarong Mu:** Investigation, Formal analysis. **Yiguo Su:** Writing – review & editing, Methodology, Investigation, Conceptualization. **Peng Wang:** Methodology, Investigation, Data curation. **Ping Bai:** Writing – original draft, Methodology, Investigation, Formal analysis, Data curation, Conceptualization.

Declaration of Competing Interest

The authors declare that they have no known competing financial interests or personal relationships that could have appeared to influence the work reported in this paper.

Data availability

Data will be made available on request.

Acknowledgements

This work was financially supported by the National Natural Science Foundation of China (Grant 22166027) and Natural Science Foundation of Inner Mongolia Autonomous Region of China (2021MS02015 and 2021MS05018).

Appendix A. Supporting information

Supplementary data associated with this article can be found in the online version at doi:10.1016/j.apcatb.2024.123882.

References

- [1] M.K. Debe, Electrocatalyst approaches and challenges for automotive fuel cells, *Nature* 486 (2012) 43–51.
- [2] J. Suntivich, K.J. May, H.A. Gasteiger, J.B. Goodenough, Y.S. Horn, A perovskite oxide optimized for oxygen evolution catalysis from molecular orbital principles, *Science* 334 (2011) 1383–1385.
- [3] T.Y. Ma, S. Dai, S.Z. Qiao, Self-supported electrocatalysts for advanced energy conversion processes, *Mater. Today* 19 (2016) 265–273.
- [4] D.S. Yu, Y.X. Hao, S.L. Han, S. Zhao, Q.C. Zhou, C.H. Kuo, F. Hu, L.L. Li, H.Y. Chen, J.W. Ren, S.J. Peng, Ultrafast combustion synthesis of robust and efficient electrocatalysts for high-current-density water oxidation, *ACS Nano* 17 (2023) 1701–1712.
- [5] I. Flis-Kabulska, J. Flis, Electroactivity of Ni-Fe cathodes in alkaline water electrolysis and effect of corrosion, *Corros. Sci.* 112 (2016) 255–263.
- [6] M. Zeng, Y.L. Liu, F.P. Zhao, K.Q. Nie, N. Han, X.X. Wang, W.J. Huang, X.N. Song, J. Zhong, Y.G. Li, Metallic cobalt nanoparticles encapsulated in nitrogen-enriched graphene shells: Its bifunctional electrocatalysis and application in zinc-air batteries, *Adv. Funct. Mater.* 26 (2016) 4397–4404.
- [7] G. Wu, K.L. More, C.M. Johnston, P. Zelenay, High-performance electrocatalysts for oxygen reduction derived from polyaniline, iron, and cobalt, *Science* 332 (2011) 443–447.
- [8] N. Wang, D. Chen, S.L. Ning, J.Y. Lao, J.C. Xu, M. Luo, W.P. Zhang, J. Chen, M. Z. Yang, F.Y. Xie, Y.S. Jin, S.H. Sun, H. Meng, Fe cluster modified Co₉S₈ heterojunction: highly efficient photoelectrocatalyst for overall water splitting and flexible zinc-air batteries, *Adv. Mater.* 36 (2024) 2306138.
- [9] X.R. Zheng, Y.H. Cao, Z. Wu, W.L. Ding, T. Xue, J.J. Wang, Z.L. Chen, X.P. Han, Y. D. Deng, W.B. Hu, Rational design and spontaneous sulfurization of NiCo(oxy) hydroxysulfides nanosheets with modulated local electronic configuration for enhancing oxygen electrocatalysis, *Adv. Energy Mater.* 12 (2022) 2103275.
- [10] Y.X. Hao, S.F. Hung, W.J. Zeng, Y. Wang, C.C. Zhang, C.H. Kuo, L.Q. Wang, S. Zhao, Y. Zhang, H.Y. Chen, S.J. Peng, Switching the oxygen evolution mechanism on atomically dispersed Ru for enhanced acidic reaction kinetics, *J. Am. Chem. Soc.* 145 (2023) 23659–23669.
- [11] J. Masa, C. Andronesi, W. Schuhmann, Electrocatalysis as the nexus for sustainable renewable energy: the gordian knot of activity, stability, and selectivity, *Angew. Chem. Int. Ed.* 59 (2020) 15298.

- [12] M.C. Zhang, K.X. Zhang, X. Ai, X. Liang, Q. Zhang, H. Chen, X.X. Zou, Theory-guided electrocatalyst engineering: from mechanism analysis to structural design, *Chin. J. Catal.* 43 (2022) 2987–3018.
- [13] C.L. Xie, Z.Q. Niu, D. Kim, M.F. Li, P.D. Yang, Surface and interface control in nanoparticle catalysis, *Chem. Rev.* 120 (2020) 1184–1249.
- [14] T.P. Zhou, N. Zhang, C.Z. Wu, Y. Xie, Surface/interface nanoengineering for rechargeable Zn-air batteries, *Energy Environ. Sci.* 13 (2020) 1132–1153.
- [15] Y.Y. Ma, Y. Yu, J.H. Wang, J. Lipton, H.N. Tan, L.R. Zheng, T. Yang, Z.L. Liu, X. J. Loh, S.J. Pennycook, L. Shen, Z.K. Kou, A.D. Taylor, J. Wang, Localizing tungsten single atoms around tungsten nitride nanoparticles for efficient oxygen reduction electrocatalysis in metal-air batteries, *Adv. Sci.* 9 (2022) 2105192.
- [16] H.M. Mao, X.B. Liu, S.Q. Wu, G.R. Sun, G.Z. Zhou, J.Q. Chi, L. Wang, Built-in electric fields and interfacial electron modulation: enhancement of oxygen reduction reaction in alkaline seawater, *Adv. Energy Mater.* (2023) 2302251.
- [17] C.H. He, Q.Q. Liu, H.M. Wang, C.F. Xia, F.M. Li, W. Guo, B.Y. Xia, Regulating oxygen electrocatalysis by built-in electric field of heterojunction electrocatalyst with modified d-band, *Small* 19 (2023) 2207474.
- [18] X. Zhao, M.J. Liu, Y.C. Wang, Y. Xiong, P.Y. Yang, J.Q. Qin, X. Xiong, Y.P. Lei, Designing a built-in electric field for efficient energy electrocatalysis, *ACS Nano* 16 (2022) 19959–19979.
- [19] S. Zhao, F. Hu, L.J. Yin, L.L. Li, S.J. Peng, Manipulating electron redistribution induced by asymmetric coordination for electrocatalytic water oxidation at a high current density, *Sci. Bull.* 68 (2023) 1389–1398.
- [20] J. Sun, H. Xue, N.K. Guo, T.S. Song, Y.R. Hao, J.W. Sun, J.W. Zhang, Q. Wang, Synergistic metal defect and surface chemical reconstruction into NiCo₂S₄/ZnS heterojunction to achieve outstanding oxygen evolution performance, *Angew. Chem. Int. Ed.* 60 (2021) 19435–19441.
- [21] D.D. Lyu, S.X. Yao, A. Ali, Z.Q. Tian, P. Tsiakaras, P.K. Shen, N. S codoped carbon matrix-encapsulated Co₉S₈ nanoparticles as a highly efficient and durable bifunctional oxygen redox electrocatalyst for rechargeable Zn-air batteries, *Adv. Energy Mater.* 11 (2021) 2101249.
- [22] D. Chen, R.H. Lu, R.H. Yu, Y.H. Dai, H.Y. Zhao, D.L. Wu, P.Y. Wang, J.W. Zhu, Z. H. Pu, L. Chen, J. Yu, S.C. Mu, Work-function-induced interfacial built-in electric fields in Os-Se₂ heterostructures for active acidic and alkaline hydrogen evolution, *Angew. Chem. Int. Ed.* 61 (2022) e202208642.
- [23] Z.K. Yuan, J. Li, M.J. Yang, Z.S. Fang, J.H. Jian, D.S. Yu, X.D. Chen, L.M. Dai, Ultrathin black phosphorus-on-nitrogen doped graphene for efficient overall water splitting: dual modulation roles of directional interfacial charge transfer, *J. Am. Chem. Soc.* 141 (2019) 4972–4979.
- [24] C.H. Kuo, Y. Tang, L.Y. Chou, B.T. Sneed, C.N. Brodsky, Z.P. Zhao, C.K. Tsung, Yolk-shell nanocrystal@ZIF-8 nanostructures for gas-phase heterogeneous catalysis with selectivity control, *J. Am. Chem. Soc.* 134 (2012) 14345–14348.
- [25] Z.Q. Liu, H. Cheng, N. Li, T.Y. Ma, Y.Z. Su, ZnCo₂O₄ quantum dots anchored on nitrogen-doped carbon nanotubes as reversible oxygen reduction/evolution electrocatalysts, *Adv. Mater.* 28 (2016) 3777–3784.
- [26] T.Y. Su, K.K. Sun, G.P. Lu, C. Cai, Synthesis of quinazolinones via a tandem hydrogen-transfer strategy catalyzed by N, S co-doped carbon-anchored Co nanoparticles, *ACS Sustain. Chem. Eng.* 10 (2022) 3872–3881.
- [27] T.Y. Su, G.P. Lu, K.K. Sun, M. Zhang, C. Cai, ZIF-derived metal/N-doped porous carbon nanocomposites: efficient catalysts for organic transformations, *Catal. Sci. Technol.* 12 (2022) 2106–2121.
- [28] Y. Hu, J.O. Jensen, W. Zhang, L.N. Cleemann, W. Xing, N.J. Bjerrum, Q.F. Li, Hollow spheres of iron carbide nanoparticles encased in graphitic layers as oxygen reduction catalysts, *Angew. Chem. Int. Ed.* 53 (2014) 3675–3679.
- [29] H. Wang, J.R. Zhao, Z. Wang, P.B. Liu, Bird-nest-like multi-interfacial MXene@SiCN_{xs}/Co/C hybrids with enhanced electromagnetic wave absorption, *ACS Appl. Mater. Interfaces* 15 (2023) 4580–4590.
- [30] Y. Wen, Z.H. Shen, J.F. Hui, H.G. Zhang, Q.S. Zhu, Co/CoSe junctions enable efficient and durable electrocatalytic conversion of polysulfides for high-performance Li-S batteries, *Adv. Energy Mater.* 13 (2023) 2204345.
- [31] S.C. Zhang, C.H. Tan, R.P. Yan, X.F. Zou, F.L. Hu, Y. Mi, C. Yan, S.L. Zhao, Constructing built-in electric field in heterogeneous nanowire arrays for efficient overall water electrolysis, *Angew. Chem. Int. Ed.* 62 (2023) 202302795.
- [32] Z.Y. Zhang, Y.Y. Tan, T. Zeng, L.Y. Yu, R.Z. Chen, N.C. Cheng, S.C. Mu, X.L. Sun, Tuning the dual-active sites of ZIF-67 derived porous nanomaterials for boosting oxygen catalysis and rechargeable Zn-air batteries, *Nano Res.* 14 (2021) 2353–2362.
- [33] H.S. Jadhav, H.A. Bandal, S. Ramakrishna, H. Kim, Critical review, recent updates on zeolitic imidazolate framework-67 (ZIF-67) and its derivatives for electrochemical water splitting, *Adv. Mater.* 34 (2022) 2107072.
- [34] Y.L. Li, B.M. Jia, Y.Z. Fan, K.L. Zhu, G.Q. Li, C.Y. Su, Bimetallic zeolitic imidazolate framework derived carbon nanotubes embedded with Co nanoparticles for efficient bifunctional oxygen electrocatalyst, *Adv. Energy Mater.* 8 (2018) 1702048.
- [35] B.Q. Xie, M.Y. Yu, L.H. Lu, H.Z. Feng, Y. Yang, Y. Chen, H.D. Cui, R.B. Xiao, J. Liu, Pseudocapacitive Co₉S₈/graphene electrode for high-rate hybrid supercapacitors, *Carbon* 141 (2019) 134–142.
- [36] T. Ouyang, X.T. Wang, X.Q. Mai, A.N. Chen, Z.Y. Tang, Z.Q. Liu, Coupling magnetic single-crystal Co₂Mo₃O₈ with ultrathin nitrogen-rich carbon layer for oxygen evolution reaction, *Angew. Chem. Int. Ed.* 59 (2020) 11948–11957.
- [37] Y. Jiang, Y.P. Deng, J. Fu, D.U. Lee, R.L. Liang, Z.P. Cano, Y.S. Liu, Z.Y. Bai, S. Hwang, L. Yang, D. Su, W.G. Chu, Z.W. Chen, Interpenetrating triphase cobalt-based nanocomposites as efficient bifunctional oxygen electrocatalysts for long-lasting rechargeable Zn-air batteries, *Adv. Energy Mater.* 8 (2018) 1702900.
- [38] W.H. Huang, T.T. Bo, S.W. Zou, Y.Z. Wang, J.M. Chen, S. Ould-Chikh, Y. Li, W. Zhou, J. Zhang, H.B. Zhang, Surface decorated Ni sites for superior photocatalytic hydrogen production, *SusMat* 2 (2022) 466–475.
- [39] T.T. Wang, P.Y. Wang, W.J. Zang, X. Li, D. Chen, Z.K. Kou, S.C. Mu, J. Wang, Nanoframes of Co₃O₄-Mo₂N heterointerfaces enable high-performance bifunctionality toward both electrocatalytic HER and OER, *Adv. Funct. Mater.* 32 (2021) 2107382.
- [40] Y.D. Liu, T. Sakthivel, F. Hu, Y.H. Tian, D.S. Wu, E.H. Ang, H. Liu, S.W. Guo, S. J. Peng, Z.F. Dai, Enhancing the d/p-band center proximity with amorphous-crystalline interface coupling for boosted pH-robust water electrolysis, *Adv. Energy Mater.* 13 (2023) 2203797.
- [41] P. Wang, P. Bai, J.R. Mu, J.F. Jing, L. Wang, Y.G. Su, N, S codoped carbon matrix-encapsulated CoFe/Co_{0.2}Fe_{0.8}S heterostructure as a highly efficient and durable bifunctional oxygen electrocatalyst for rechargeable zinc-air batteries, *J. Colloid Interface Sci.* 642 (2023) 1–12.
- [42] Y.T. He, X.X. Yang, Y.S. Li, L.T. Liu, S.W. Guo, C.Y. Shu, F. Liu, Y.N. Liu, Q. Tan, G. Wu, Atomically dispersed Fe-Co dual metal sites as bifunctional oxygen electrocatalysts for rechargeable and flexible Zn-air batteries, *ACS Catal.* 12 (2022) 1216–1227.
- [43] L. Yan, H.Y. Wang, J.L. Shen, J.Q. Ning, Y.J. Zhong, Y. Hu, Formation of mesoporous Co/CoS/Metal-N-C@S, N-codoped hairy carbon polyhedrons as an efficient trifunctional electrocatalyst for Zn-air batteries and water splitting, *Chem. Eng. J.* 403 (2021) 126385.
- [44] D.N. Ding, K. Shen, X.D. Chen, H.R. Chen, J.Y. Chen, T. Fan, R.F. Wu, Y.W. Li, Multi-level architecture optimization of MOF-templated Co-based nanoparticles embedded in hollow N-doped carbon polyhedra for efficient OER and ORR, *ACS Catal.* 8 (2018) 7879–7888.
- [45] Q.Q. Cheng, S.B. Han, K. Mao, C. Chen, L.J. Yang, Z.Q. Zou, M. Gu, Z. Hu, H. Yang, Co nanoparticle embedded in atomically-dispersed Co-N-C nanofibers for oxygen reduction with high activity and remarkable durability, *Nano Energy* 52 (2018) 485–493.
- [46] H. Jiang, J.X. Gu, X.S. Zheng, M. Liu, X.Q. Qiu, L.B. Wang, W.Z. Li, Z.F. Chen, X. B. Ji, J. Li, Defect-rich and ultrathin N doped carbon nanosheets as advanced trifunctional metal-free electrocatalysts for the ORR, OER and HER, *Energy Environ. Sci.* 12 (2019) 322–333.
- [47] H.J. Huang, A. Huang, D. Liu, W.T. Han, C.H. Kuo, H.Y. Chen, L.L. Li, H. Pan, S. J. Peng, Tailoring oxygen reduction reaction kinetics on perovskite oxides via oxygen vacancies for low-temperature and knittable zinc-air batteries, *Adv. Mater.* 35 (2023) 2303109.
- [48] L.L. Bi, X.P. Gao, L.J. Zhang, D.J. Wang, X.X. Zou, T.F. Xie, Enhanced photocatalytic hydrogen evolution of NiCoP/g-C₃N₄ with improved separation efficiency and charge transfer efficiency, *ChemSusChem* 11 (2018) 276–284.
- [49] S. Zhao, Y. Wang, Y.X. Hao, L.J. Yin, C.H. Kuo, H.Y. Chen, L.L. Li, S.J. Peng, Lewis acid driving asymmetric interfacial electron distribution to stabilize active species for efficient neutral water oxidation, *Adv. Mater.* (2023) 2308925.
- [50] H.Z. Yu, S.Q. Zhu, Y.X. Hao, Y.M. Chang, L.L. Li, J. Ma, H.Y. Chen, M.H. Shao, S. J. Peng, Modulating local interfacial bonding environment of heterostructures for energy-saving hydrogen production at high current densities, *Adv. Funct. Mater.* 33 (2023) 2212811.
- [51] S.H. Liu, Z.Y. Wang, S. Zhou, F.J. Yu, M.Z. Yu, C.Y. Chiang, W.Z. Zhou, J.J. Zhao, J. S. Qiu, Metal-organic-framework-derived hybrid carbon nanocages as a bifunctional electrocatalyst for oxygen reduction and evolution, *Adv. Mater.* 29 (2017) 1700874.
- [52] W.J. Kang, Y. Feng, Z. Li, W.Q. Yang, C.Q. Cheng, Z.Z. Shi, P.F. Yin, G.R. Shen, J. Yang, C.K. Dong, H. Liu, F.X. Ye, X.W. Du, Strain-activated copper catalyst for pH-universal hydrogen evolution reaction, *Adv. Funct. Mater.* 32 (2022) 2112367.
- [53] K.X. Ding, J.G. Hu, J. Luo, L.M. Zhao, W. Jin, Y.P. Liu, Z.H. Wu, G.Q. Zou, H. S. Hou, X. B. Ji, Robust electronic correlation of Co-CoN₄ hybrid active sites for durable rechargeable Zn-air batteries, *Adv. Funct. Mater.* 32 (2022) 2207331.
- [54] R.B. Ghising, U.N. Pan, D.R. Paudel, M.R. Kandel, N.H. Kim, J.H. Lee, A hybrid trimetallic-organic framework-derived N, C co-doped Ni-Fe-Mn-P ultrathin nanosheet electrocatalyst for proficient overall water-splitting, *J. Mater. Chem. A* 10 (2022) 16457–16467.
- [55] L. Yang, X.F. Zeng, W.C. Wang, D.P. Cao, Recent progress in MOF-derived, heteroatom-doped porous carbons as highly efficient electrocatalysts for oxygen reduction reaction in fuel cells, *Adv. Funct. Mater.* 28 (2018) 1704537–1704558.
- [56] X.T. Zhang, Z.Y. Zhu, Y.B. Tan, K. Qin, F.X. Ma, J.H. Zhang, Co, Fe codoped holey carbon nanosheets as bifunctional oxygen electrocatalysts for rechargeable Zn-air batteries, *Chem. Commun.* 57 (2021) 2049–2052.
- [57] L.T. Song, T.L. Zheng, L.R. Zheng, B. Lu, H.Q. Chen, Q.G. He, W.Z. Zheng, Y. Hou, J.L. Lian, Y. Wu, J. Chen, Z.Z. Ye, J.G. Lu, Cobalt-doped basic iron phosphate as bifunctional electrocatalyst for long-life and high-power-density rechargeable zinc-air batteries, *Appl. Catal. B: Environ.* 300 (2022) 120712.
- [58] K.L. Zhou, Z.L. Wang, C.B. Han, X.X. Ke, C.H. Wang, Y.H. Jin, Q.Q. Zhang, J.B. Liu, H. Wang, H. Yan, Platinum single-atom catalyst coupled with transition metal/metal oxide heterostructure for accelerating alkaline hydrogen evolution reaction, *Nat. Commun.* 12 (2021) 3783.
- [59] J.Y. Li, J. Hu, M.K. Zhang, W.Y. Gou, S. Zhang, Z. Chen, Y.Q. Qu, Y.Y. Ma, A fundamental viewpoint on the hydrogen spillover phenomenon of electrocatalytic hydrogen evolution, *Nat. Commun.* 12 (2021) 3502.
- [60] Y.Y. Guo, P.F. Yuan, J.N. Zhang, Y.F. Hu, I.S. Amiin, X. Wang, J.G. Zhou, H.C. Xia, Z.B. Song, Q. Xu, S.C. Mu, Carbon nanosheets containing discrete Co-N_x-B_y-C active sites for efficient oxygen electrocatalysis and rechargeable Zn-air batteries, *ACS Nano* 12 (2018) 1894–1901.